Phase-Adaptive Dynamical Decoupling Methods for Robust Spin-Spin Dynamics in Trapped Ions

Lijuan Dong,[1,2] Iñigo Arrazola,[2,*] Xi Chen,[1,2] and Jorge Casanova[2,3]

[1] *International Center of Quantum Artificial Intelligence for Science and Technology (QuArtist) and Department of Physics, Shanghai University, Shanghai 200444, China*

[2] *Department of Physical Chemistry, University of the Basque Country UPV/EHU, Apartado 644, Bilbao 48080, Spain*

[3] *IKERBASQUE, Basque Foundation for Science, Plaza Euskadi 5, Bilbao 48080, Spain*

(Received 14 September 2020; revised 17 December 2020; accepted 26 February 2021; published 18 March 2021)

Quantum platforms based on trapped ions are the main candidates to build a quantum hardware with computational capacities that largely surpass those of classical devices. Among the available control techniques in these setups, pulsed dynamical decoupling (pulsed DD) has been revealed as a useful method to process the information encoded in ion registers, whilst minimizing the environmental noise over them. In this work, we incorporate a pulsed DD technique that uses random pulse phases, or correlated pulse phases, to significantly enhance the robustness of entangling spin-spin dynamics in trapped ions. This procedure was originally conceived in the context of nuclear magnetic resonance for nuclear spin detection purposes, and here we demonstrate that the same principles apply for robust quantum-information processing in trapped-ion settings.

DOI: 10.1103/PhysRevApplied.15.034055

I. INTRODUCTION

The controlled generation of arbitrary quantum states, their subsequent processing via quantum operations, and their adequate preservation in quantum bits (qubits) are recurrent duties in the quantum-computing area [1,2]. In platforms such as superconducting circuits and trapped ions [3,4], bosonic modes that couple several qubits enables construction of arbitrary quantum states via entangling gates among several qubits. In particular, in setups based on trapped ions, qubits are encoded in the internal degrees of freedom of the ions, whilst collective vibrational normal modes of the ion chain are used as a bosonic quantum bus. This mediation, along with the ability to control the internal states of the atoms with laser and/or microwave (MW) radiation [5,6], led to high-fidelity quantum-information processing in the form of entangling gates [7,8], or quantum simulations of many-body spin systems [9–15].

In trapped ions, qubit-boson coupling is typically achieved with a laser that supplies the energy gap between the ion qubit and specific vibrational modes [5]. Here, the strength of the qubit-boson interaction is proportional to the Lamb-Dicke (LD) factor η. This is given by the ratio between the width of the motional ground-state wave function, and the wavelength of the employed laser. Often, the LD factor takes values below 0.1 [5], such as $\eta = 0.044$ in Ref. [16] or $\eta = 0.089$ in Ref. [17]. On the other hand, one can also use trapped ions that encode a qubit with an energy splitting lying on the MW regime. One example of this is the $^{171}Yb^{+}$ ion [18,19]. In this scenario, MW fields can exert local operations on the qubit states, but fail to induce a coupling with the vibrational modes of the ion chain. This is due to the effective LD factor of the qubit-boson interaction that amounts to approximately 10^{-7} as a consequence of the long wavelength of the MW radiation fields. Solutions to this problem involve introducing either static [20–25] or oscillating [26–30] magnetic field gradients. In current setups, these gradients induce an effective LD factor, which is approximately one order of magnitude smaller than those in laser-based systems. For example, the MW scheme in Ref. [31] leads to a LD factor $\eta = 0.0041$. However, larger values for the LD factor are expected to be reached in new MW setups [31]. From a different perspective, it is noteworthy to mention that the use of MW radiation has several advantages with respect to lasers. On the one hand, MW technology is easier to control and incorporate in scalable trap designs [32]. On the other hand, MW radiation avoids spontaneous scattering of photons, which is a fundamental limitation in laser-based ion setups [7,8]. Furthermore, long-wavelength radiation is less sensitive to phase perturbations due to, for example, mirror vibrations or geometrical drifts.

*inigo.arrazola@ehu.eus

In another vein, qubit-boson coupling can be achieved in two different fashions. On the one hand, a transversal coupling of the form $H_x = \eta\Omega(a + a^\dagger)\sigma_x$ is achieved in laser-driven interactions [33] or using magnetic field gradients [34]. On the other hand, longitudinal couplings of the form $H_z = \eta\Omega(a + a^\dagger)\sigma_z$ are produced with lasers [12,33,35], as well as with static [20] or oscillating [34] magnetic field gradients. A notable difference between transversal and longitudinal couplings is that the latter commutes with the system's bare Hamiltonian. This is defined by the $\sigma_z|e\rangle = |e\rangle$ and $\sigma_z|g\rangle = -|g\rangle$ basis states. As a consequence, longitudinal couplings enable a straightforward application of pulsed DD techniques [36–38] while, typically, continuous DD schemes are pursued for transversal couplings [39–43]. Both techniques, pulsed and continuous, are devoted to cancel errors leading to qubit dephasing. However, pulsed DD schemes offer a superior performance against environmental fluctuations, as well as in front of errors on the drivings.

Besides protecting the system from environmental noise, DD techniques are routinely employed to exert control on the system evolution. For example, a qubit can be dynamically decoupled from environmental signals, except from those whose frequencies lie on a certain energy window. This enables the coupling of a qubit with specific signals, leading to applications in quantum sensing [44–49]. In trapped ions, DD has been used to accomplish high-fidelity entangling gates [31,50]. Furthermore, pulsed DD has been proposed as a generator of fast gates with MW-driven ions [51].

In this paper we demonstrate that phase-adaptive DD methods, previously introduced in the context of nuclear magnetic resonance [52,53], can be incorporated to trapped-ion systems to achieve significantly enhanced robustness in quantum-information processing via spin-spin dynamics. In particular, phase-adaptive DD methods use either random or correlated pulse phases to remove common experimental errors. We want to remark that, to vary the phase of each delivered pulse in a sequence represents a minimal added experimental cost while, in contrast, we show that it leads to a large improvement in the fidelity of the implemented quantum gates. We choose the system of MW-driven trapped ions in a static magnetic field gradient to illustrate our proposal, although the results presented here can be incorporated to any setup presenting longitudinal qubit-boson coupling such as superconducting circuits [54,55] or ions in Penning traps [56]. In addition, we notice that in this work we consider MW Rabi frequencies orders of magnitude smaller than those in Ref. [51], making our proposal experimentally accesible for current setups, at the price of longer gate times.

The paper is organized as follows: In Sec. II we review how the longitudinal coupling in trapped ions leads to effective spin-spin interactions that can be exploited for quantum logic, or to implement quantum simulations. In Sec. III we show that DD pulse sequences can be combined with these spin-spin interactions, achieving protection against environmental errors. We also find the consequences of using realistic finite-width MW pulses. In particular, we demonstrate that these pulses lead to a reduction of the effective spin-spin coupling strength. We consider this effect in our newly designed sequences that use phase-adaptive methods. Finally, in Sec. IV we incorporate phase-adaptive DD methods to generate robust spin-spin interactions in trapped-ion setups with longitudinal coupling. More specifically, via detailed numerical simulations we prove that phase-adaptive DD schemes offer a significantly improved fidelity in quantum-information processing with a minimal extra experimental cost (this is the appropriate control of each pulse phase). This demonstrates the usefulness of the presented method.

II. QUANTUM LOGIC WITH LONGITUDINAL COUPLING

In this section, we briefly review the type of quantum dynamics one can get by exploiting trapped ions with longitudinal coupling. We consider a chain of N trapped ions, placed in the axial (z) direction of a linear trap with an axial trapping frequency ν, along a magnetic field gradient g_B in the same direction. The Hamiltonian that describes this situation is (here, and throughout the paper, $H \to H/\hbar$, where $\hbar$ is the reduced Planck constant, meaning the Hamiltonians are given in units of angular frequency)

$$H_{\rm sys} = \sum_{j=1}^{N} \frac{\omega_j}{2}\sigma_j^z + \sum_{m=1}^{N} \nu_m a_m^\dagger a_m + 2\sum_{j,m} \eta_{jm}\nu_m(a_m + a_m^\dagger)|e\rangle\langle e|_j, \quad (1)$$

where $\sigma_j^z = |e\rangle\langle e|_j - |g\rangle\langle g|_j$, $\omega_j = \omega_0 + \gamma_e B_j/2$ is the frequency of qubit j, related with the value of the magnetic field in the ion's equilibrium position z_j^0, i.e., $B_j = B_0 + g_B z_j^0$. Also, $\eta_{jm} = b_{jm}\gamma_e g_B/4\nu_m\sqrt{\hbar/2M_I\nu_m}$, M_I is the mass of an ion, γ_e is the electronic gyromagnetic ratio, ν_m and $a_m^\dagger(a_m)$ are the frequency and the creation (annihilation) operators associated with the mth normal vibrational mode, and b_{jm} is a coefficient that relates this mode with the jth ion's displacement in the z direction [57].

The Schrödinger equation associated to Hamiltonian (1) can be analytically solved, and it describes an effective spin-spin interaction mediated by the vibrational modes [20,58,59]. In order to see this, we first move to a rotating frame with respect to the first two terms in Eq. (1). The resulting Hamiltonian reads [33]

$$H_{\rm sys}^I = \sum_{j,m} \eta_{jm}\nu_m(a_m e^{-i\nu_m t} + a_m^\dagger e^{i\nu_m t})(1 + \sigma_j^z). \quad (2)$$

The time-evolution operator associated to Hamiltonian (2) has the form $U = U_S U_F$, where

$$U_F(t) = \prod_{j,m}^{N} \exp\{[\alpha_{jm}(t)a_m^\dagger - \alpha_{jm}^*(t)a_m](1+\sigma_j^z)\} \quad (3)$$

is a product of spin-dependent displacement operators with $\alpha_{jm}(t) = -\eta_{jm}(e^{i\nu_m t} - 1)$, and

$$U_S(t) = \exp\left[-i\sum_{i,j}^{N}\theta_{ij}(t)(1+\sigma_i^z)(1+\sigma_j^z)\right] \quad (4)$$

is a spin-spin operator, where $\theta_{ij}(t) = \sum_m \eta_{im}\eta_{jm}[\nu_m t - \sin(\nu_m t)]$. If $\eta_{jm} \ll 1$, the U_F propagator can be ignored as $\alpha_{jm}(t)$ is a bounded quantity. Conversely, the quantity $\theta_{ij}(t)$ that appears in U_S grows linearly with time t leading to an effective spin-spin gate that is described by the Hamiltonian

$$H_{\text{eff}}^I = -\frac{\delta}{2}S^z - \sum_{i,j}^{N} J_{ij}\sigma_i^z\sigma_j^z, \quad (5)$$

where $\delta = \hbar\gamma_e g_B/2M_I\nu$, $S^\alpha = \sum_j^N \sigma_j^\alpha$, and $J_{ij} = \sum_m \nu_m \eta_{im}\eta_{jm}$. Notice that the effective Hamiltonian in Eq. (5) does not contain bosonic degrees of freedom.

Equation (5) corresponds to an Ising model with a longitudinal field [60]. Interestingly, the dynamics of these types of Ising Hamiltonians can be combined with $\pi/2$ pulses and, with the help of the Suzuki-Trotter expansion [61], it leads to the simulation of distinct spin models [62,63]. In addition, the Ising model describes entangling operations between, e.g., two ions in a chain [23]. To demonstrate this, we assume that all ions, except the ith and jth, are in the qubit's ground state $|g\rangle$. In that case, Hamiltonian (5) reduces to

$$H_{\text{eff}}^I = -\frac{\delta_i}{2}\sigma_i^z - \frac{\delta_j}{2}\sigma_j^z - J\sigma_i^z\sigma_j^z, \quad (6)$$

where $\delta_i = 4\sum_{m=1}^N \nu_m\eta_{im}(\eta_{im}+\eta_{jm})$, $\delta_j = 4\sum_{m=1}^N \nu_m\eta_{jm}(\eta_{jm}+\eta_{im})$ (notice that a $J_0\sigma_j^z\sigma_k^z$ term contributes to the energy of the jth qubit with $-J_0$ if the kth qubit is projected in $|g\rangle$ state) and $J = 2\sum_{m=1}^N \nu_m\eta_{im}\eta_{jm}$. Now, by preparing the initial state $|++\rangle$ ($\sigma^x|\pm\rangle = \pm|\pm\rangle$) for the ith and jth qubits and in an interaction picture with respect to the first two terms in Eq. (6), the Bell state $|++\rangle + i|--\rangle$ (up to normalization) is obtained after a time $t_G = \pi/4J$. Regarding the fidelity of this procedure, in the absence of error sources this is only limited by the accuracy of the approximation $U_F \approx 1$. In particular, the Bell-state fidelity can be bounded by

$$F \approx 1 - \frac{1}{2}\Big[\sum_{m,m'}\Theta_{mm'}(2\bar{n}_m+1)(2\bar{n}_{m'}+1)\Big], \quad (7)$$

where $\bar{n}_m$ is the average number of phonons in mode m and $\Theta_{mm'} = |\alpha_{im}|^2|\alpha_{im'}|^2 + |\alpha_{jm}|^2|\alpha_{jm'}|^2 + 4\alpha_{im}\alpha_{jm}^*\alpha_{im'}\alpha_{jm'}^*$ (see Appendix A for further details on the calculation). Assuming that $\alpha_{jm}(t) = 2\eta_{jm}$, which maximizes the value of $|\alpha_{jm}(t)|$, we obtain that, for $N = 2$ and $\bar{n}_m \approx 1$,

$$1 - F \lesssim 98\eta^4, \quad (8)$$

where $\eta = \gamma_e g_B/4\nu\sqrt{\hbar/2M_I\nu}$ is the effective LD factor (see Appendix B for further details on the obtention of the bound). For two $^{171}Yb^+$ ions with a trapping frequency of $\nu \approx (2\pi)\times 220$ kHz, the infidelity due to the residual spin-boson coupling is of the order of 10^{-3} for $g_B \approx 150$ T/m ($\eta \approx 0.056$) and of 10^{-5} for $g_B \approx 50$ T/m ($\eta \approx 0.018$). These conditions lead to gates times, t_G, of $t_G \approx 270$ μs and $t_G \approx 2.65$ ms, respectively. Faster gates can be achieved by driving the system with continuous drivings [39,41,43] or with fast π pulses [51]. In these cases, $|\alpha_{jm}(t)| \leq 2\eta_{jm}$ does not hold true [thus Eq. (8) neither] however, Eq. (7) is still valid to quantify the infidelity due to residual spin-boson coupling.

As shown in Ref. [64], DD schemes are required to protect spin-spin dynamics against environmental noise. This can be achieved by applying sequences of π pulses upon the qubits. However, these pulses also suffer from control errors (namely, deviations in their Rabi frequencies as well as detuning errors) whose effect on the spin-spin dynamics could be even more harmful than the noise introduced by the environment. Hence, DD sequences that are robust against these types of errors are highly desirable. These types of sequences have been considered in Ref. [51] to generate fast entangling gates, with $\eta \gtrsim 0.05$ and fast π pulses, i.e., with Rabi frequencies much larger than the trapping frequency. In that regime, the condition $U_F(t_G) = 1$ is pursued by varying the time between pulses, and how to achieve this condition for more than two ions is still an unsolved problem [51]. Here, we consider low-power MW pulses with Rabi frequencies below the trapping frequency and $\eta \approx 0.01$. In this regime corresponding to current experimental setups [23,31] $U_F \approx 1$ is a good approximation, and, thus, the extension to more than two ions is straighforward. In the next section, we describe how DD sequences can be applied in this regime and analyse the effect of using low-power MW pulses for quantum-information processing.

III. PROTECTED MULTIQUBIT DYNAMICS

For applying a pulsed DD sequence to the system described in the previous section, the ions have to be

addressed with MW radiation. This requires a multitone MW signal that involves all qubit resonance frequencies ω_j and leading to the Hamiltonian

$$H = H_{\rm sys} + \Omega(t)\sum_{j=1}^{N} S^x \cos(\omega_j t - \phi). \tag{9}$$

For simplicity, here we assume that the Rabi frequency $\Omega(t)$ and the phase ϕ are the same for all ions. In an interaction picture with respect to $\sum_j \omega_j/2\sigma_j^z + \sum_m \nu_m a_m^\dagger a_m$, and neglecting terms rotating at frequencies $2\omega_j$ and $|\omega_j - \omega_i|$, we have

$$H^I = H^I_{\rm sys} + \frac{\Omega(t)}{2}(S^+ e^{i\phi} + S^- e^{-i\phi}). \tag{10}$$

In the case of pulsed DD techniques, MW radiation is delivered stroboscopically as π pulses, such that $\Omega(t)$ is zero except when the pulse is applied, see Fig. 1(a) for a specific example. As a consequence, the qubits get protected with respect to errors of the type $\sum_i \epsilon_i/2\sigma_i^z$ that may be caused by, for example, variations on the magnetic field B_0. Contrary to Hamiltonian (2), the time-evolution operator associated to Eq. (10) does not have an analytical form. In this manner, numerical simulations are required to study the performance of DD schemes to produce protected spin-spin dynamics.

In this work, we consider the XY8 pulse sequence, which is formed by blocks of eight pulses with an interpulse spacing τ and with phases $\vec{\phi} = \{0, \pi/2, 0, \pi/2, \pi/2, 0, \pi/2, 0\} + \Phi$, where Φ is a global phase that adds to those of all pulses. In Fig. 1(a), the specific case of an XY8 block is sketched. A pulse sequence may be formed by blocks with the same global phase Φ, as in Fig. 1(c), or different phases Φ_s, as in Fig. 1(d). In this section, we consider the same phase Φ for all blocks, while in Sec. IV we prove the advantage of using different global phases for improved robustness against environmental and control errors.

In Fig. 2(a)we plot the fidelity with respect to the state generated by $H = \sum_{i,j} J_{ij}\sigma_i^z\sigma_j^z$ at $t_G = \pi/8\max(|J_{ij}|)$ (for $N = 2$, this is a Bell state) as a function of an unwanted energy shift ϵ, and for a number of ions $N = 2$ (solid) and $N = 6$ (dashed). In particular, we consider a scenario involving π pulses, as well as the pulse-free case. The parameters we use in our simulations are $\nu = (2\pi)\times 220$ kHz and $\eta = 0.018$, for which the ideal gate times are $t_G = 2.62$ ms and $t_G = 4.50$ ms for $N = 2$ and $N = 6$, respectively. At this point we anticipate that, when combining the spin-spin Hamiltonian with finite-width π pulses, a total time t_G will no longer be sufficient in order to obtain the desired state. Furthermore, the corresponding values of J_{ij} for $N = 6$ are plotted in Fig. 2(b), while further details about their calculation are in Appendix C.

In the case of $N = 2$, we compare the evolution produced by the ideal Hamiltonian $H = \sum_{i,j} J_{ij}\sigma_i^z\sigma_j^z$ and the

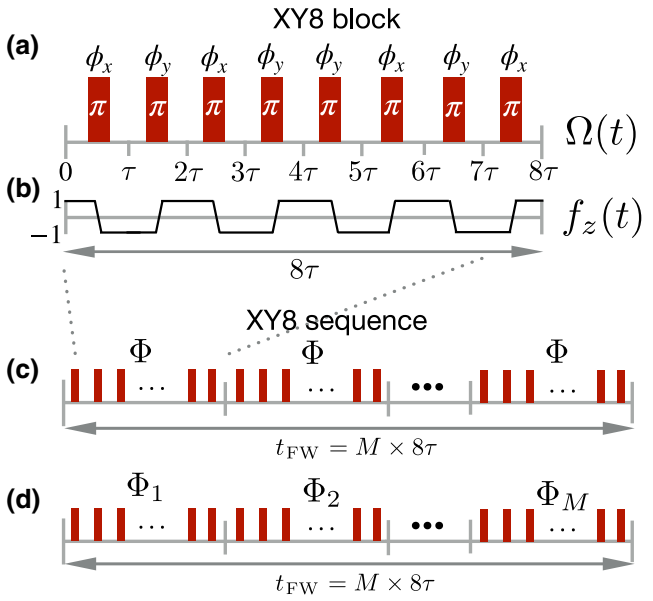

FIG. 1. (a) XY8 pulse block with duration 8τ. The Rabi frequency takes the value Ω while applying the π pulse, i.e., in the red region. The relative phase between the pulses changes according to $\phi_x = 0 + \Phi$ and $\phi_y = \pi/2 + \Phi$. (b) Modulation function $f_z(t)$ corresponding to a single XY8 block. (c) The basic block shown in (a) is repeated to construct a longer sequence. In this case, the same global phase is chosen for all blocks. (d) The global phases Φ_s can be chosen to be different for each block s.

Hamiltonian (10) that includes realistic finite-width pulses where, in addition, each bosonic mode is in a thermal state with $\bar{n}_m = 1$. For $N = 6$, due to the computational overhead of simulating six bosonic modes, we consider all motional modes to be in their respective ground states. In Fig. 2(a), the fidelity curves in the pulse-free cases (solid-blue and dashed-blue curves) drop down to 99% at $\epsilon \approx (2\pi)\times 5$ Hz. In contrast, in the pulsed cases (solid-red and dashed-red curves), the fidelity falls to 99% for $\epsilon \approx (2\pi)\times 1$ kHz, which represents an improvement factor approximately equal to 200. Further details regarding our simulations are for the pulsed case with $N = 2$, we consider a sequence with 64 pulses (this is eight XY8 blocks) where each π pulse is implemented with a Rabi frequency $\Omega = (2\pi)\times 40$ kHz leading to a π-pulse time of 12.5 μs. In addition, an interpulse spacing of $\tau = 50.28$ μs is employed. For $N = 6$, the interpulse spacing is $\tau = 146.56$ μs, and we consider a sequence of 32 π pulses (i.e., four XY8 blocks) with $\Omega = (2\pi)\times 60$ kHz leading to a π-pulse time approximately equal to 8.3 μs. The final times for both sequences that use finite-width pulses are $t_{\rm FW} = 3.22$ ms (64×50.28 μs) for the case with $N = 2$, and $t_{\rm FW} = 4.69$ ms (32×146.56 μs) for $N = 6$.

It is worthwhile to note that the latter final times $t_{\rm FW}$ do not correspond to the ideal final times $t_G = 2.62$ ms and $t_G = 4.50$ ms. This is because, during the application of

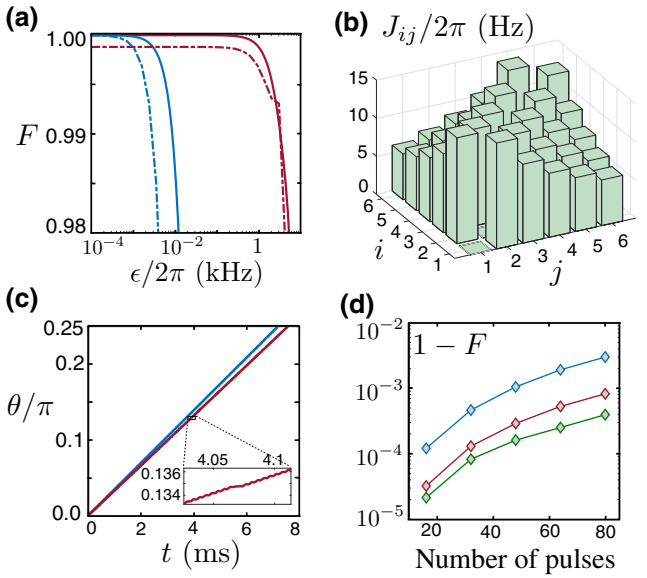

FIG. 2. (a) Fidelity with respect to the state generated by $H = \sum_{i,j} J_{ij}\sigma_i^z\sigma_j^z$ at $t_G = \pi/8\max(|J_{ij}|)$ as a function of the strength of the unwanted shift ϵ and for $N = 2$ (solid curves) and $N = 6$ (dashed curves). The pulsed cases (red curves) are protected up to $\epsilon \approx (2\pi) \times 1$ kHz, while the fidelity for the pulse-free cases (blue curves) takes values below 99% around $\epsilon \approx (2\pi) \times 5$ Hz; an improvement factor approximately equal to 200 is obtained in the pulsed case. Due to the effect of realistic finite-width pulses, the pulsed case for $N = 6$ gets a fidelity of $F \approx 99.8\%$ fidelity for $\epsilon \to 0$. (b) J_{ij} matrix elements for $N = 6, \eta = 0.018$ and $\nu = (2\pi) \times 220$ kHz. (c) Accumulated two-qubit phase versus time for $\eta = 0.0113$, $\nu = (2\pi) \times 200$ kHz, and $\Omega = (2\pi) \times 40$ kHz. The pulse-free case (blue) reaches $\theta = \pi/4$ around $t_G \approx 7.1$ ms, while for the pulsed case (red) it takes $t_{\rm FW} \approx 7.5$ ms. Inset: phase accumulation around $t \approx 4.05 - 4.1$ ms. It can seen that phase accumulation stops during the application of a π pulse leading to a plateau effect, which lasts approximately 12.5 μs. (d) Bell-state infidelity for $\eta = 0.0113$, $\nu = (2\pi) \times 200$ kHz and for the XY8 pulse sequence with 16, 32, 48, 64, and 80 pulses. The cases with Rabi frequencies $\Omega = (2\pi) \times (20, 40,$ and $60)$ kHz are shown with blue, red, and green colors, respectively. Due to the effect of transversal terms in Eq. (11), the fidelity decreases when increasing the number of pulses or decreasing Ω.

a π pulse, the phase accumulation stops. Hence, for the pulsed cases, to achieve the same state as the one generated by the error-free Hamiltonian $H = \sum_{i,j} J_{ij}\sigma_i^z\sigma_j^z$ at t_G requires a longer time $t_{\rm FW}$. This effect is studied in more detail later. Another aspect that can be observed in Fig. 2(a) is that, although the pulsed case is still far less sensitive with respect to the unwanted shifts than the pulsed-free case, the fidelity of the achieved state is, in the best case, around 99.8% (note that the dashed-red curve does not reach the value 1 when $\epsilon \to 0$). Later, we specify how this fidelity can be improved.

The previously commented effects, i.e., the reduction in the fidelity and the modified phase accumulation, are caused by the application of finite-length MW pulses. To show this, in Eq. (10), we move to a rotating frame with respect to $\Omega(t)/2(S^+e^{i\phi} + S^-e^{-i\phi})$, which leads to the following Hamiltonian

$$\tilde{H}^I_{\rm sys} = \sum_{j,m} \eta_{jm}\nu_m(a_m e^{-i\nu_m t} + \text{H.c.})[1 + f_z(t)\sigma_j^z + f_\perp(t)\sigma_j^\perp], \tag{11}$$

where $f_z(t) = \cos[\int_{t_0}^t \Omega(t')dt']$, $f_\perp(t) = \sin[\int_{t_0}^t \Omega(t')dt']$, and $\sigma_j^\perp = -i(\sigma_j^+ e^{i\phi} - \sigma_j^- e^{-i\phi})$. During a π pulse, the function $f_z(t)$ changes from 1 to -1, see Fig. 1(b), while $f_\perp(t)$ evolves from 0 to 0. Furthermore, when the system is not being driven, $f_z(t)$ is 1 or -1 depending on the number of applied pulses, while $f_\perp(t) = 0$. Now, for the sake of clarity in the presentation, we neglect the effect of the transversal terms—i.e., those that appear multiplying $\sigma_j^\perp$ in Eq. (11)—as they are acting only during the π-pulse execution. However, they are included in our numerical simulations, and their impact on the dynamics is discussed. Finally, the spin-spin effective Hamiltonian takes the following form:

$$\tilde{H}^I_{\rm eff} = -\sum_{i<j}^N J_{ij}(t)\sigma_i^z\sigma_j^z, \tag{12}$$

where $J_{ij}(t) = d\theta_{ij}(t)/dt$ with

$$\theta_{ij}(t) = \sum_m \nu_m^2\eta_{im}\eta_{jm}\,\text{Im}\int_0^t\int_0^{t'} e^{i\nu_m(t'-t'')}f_z(t')f_z(t'')dt'dt''. \tag{13}$$

Note that, in the previous expression "Im" means the imaginary part of the subsequent integral.

Most of the time, $f_z(t)$ takes the value 1 or -1, resulting in a spin-spin coupling equivalent to the one in Eq. (5), i.e., $J_{ij}(t) = J_{ij}$ and the phase $\theta_{ij}(t) = J_{ij} \times t$. However, during the application of a π pulse, $f_z(t)$ is not constant. The result is that the phase accumulated during t_π, i.e., the duration of the π pulse, is smaller than $J_{ij} \times t_\pi$ [the latter is the phase that would be accumulated in during t_π in case $f_z(t)$ would take a constant value]. In practice, this implies that, when including realistic finite-width π pulses, a longer time is needed to generate the final value for the phase than in the pulse-free case. This is shown in Fig. 2(c) for the case of two ions ($N = 2$). In particular, we find that preparing a Bell state, this is to achieve the phase $\theta = \pi/4$, takes longer for the pulsed case (solid-red curve) than for the pulse-free case in solid-blue. As a final comment, in Fig. 2(a) the appropriate final times, $t_{\rm FW}$, for the pulsed cases are calculated using Eq. (13).

Regarding the transversal terms in Eq. (11) we neglect them in the presentation since they are nonzero only during the application of π pulses. However, these transversal

terms have a noticeable effect when the number of qubits is large, as well as with a growing number of applied MW pulses, and with significant pulse lengths (i.e., when the Rabi frequency of each pulse is small). In particular, these transversal terms are responsible for the $F \approx 99.8\%$ fidelity observed in Fig. 2(a) for the case with $N = 6$. Here, the number of applied pulses is actually larger than in the $N = 2$ case (note each ion is being addressed with a different MW pulse). This issue can be solved by introducing shorter π pulses, i.e., with larger Rabi frequency. In Appendix D, we show how the $F \approx 99.8\%$ fidelity can be improved up to 99.99% by using a larger Rabi frequency $\Omega = (2\pi) \times 160$ kHz and lowering the LD factor (see Fig. 4).

To further study the effect of these transversal terms, in Fig. 2(d) we plot the Bell-state infidelity for sequences with a different number of pulses and applied in two ions ($N = 2$) without any unwanted shift ϵ. More specifically, we compare XY8 sequences with Rabi frequencies $\Omega = (2\pi) \times 20$ kHz (blue curves), $\Omega = (2\pi) \times 40$ kHz (red curves), and $\Omega = (2\pi) \times 60$ kHz (green curves). In the simulations, we choose $\eta = 0.0113$ ($g_B = 26.8$ T/m) and $\nu = (2\pi) \times 200$ kHz, and calculate the evolution according to Hamiltonian (10) with each bosonic mode starting in a thermal state with $\bar{n}_m = 0.5$.

Using Eq. (13), one can obtain the final time t_{FW} that corresponds to a Bell state for the different Rabi frequencies. Notice that when decreasing the value of Ω, the final fidelity decreases. We also notice that, for the Bell-state preparation, introducing more pulses is detrimental due to the accumulated effect of the transversal terms. However, sequences with more pulses may offer an enhanced protection against environmental and control errors than their counterparts with a reduced number of pulses. Hence, in a real experimental scenario, a trade-off between these two effects ought to be found, in order to achieve the best possible fidelities.

Finally, we consider the effect that the heating of the vibrational modes may have in the final fidelity of the prepared Bell states. For some gates this is a major source of infidelity, and specific techniques have been developed to gain robustness against this type of error [65–67]. To account for the effect of motional heating we use a master equation of the form

$$\dot{\rho} = -i[H, \rho] + \sum_{m=1}^{2} \mathcal{L}_m(\rho), \tag{14}$$

where ρ is the density matrix, H is Eq. (10) in the Schrödinger picture, and the dissipative terms are

$$\mathcal{L}_m(\rho) = \frac{\Gamma_m}{2}(\bar{N}_m + 1)(2a_m\rho a_m^\dagger - a_m^\dagger a_m\rho - \rho a_m^\dagger a_m) + \frac{\Gamma_m}{2}\bar{N}_m(2a_m^\dagger\rho a_m - a_m a_m^\dagger\rho - \rho a_m a_m^\dagger), \tag{15}$$

with $\bar{N}_m = [\exp(\hbar\nu_m/k_BT) - 1]^{-1}$. Here, $\dot{\bar{n}}_m \approx \Gamma_m\bar{N}_m$ is the heating rate for the mth mode and $T = 300$ K. For the parameters considered in Fig. 2(d), $\eta = 0.0113$ and $\nu = (2\pi) \times 200$ kHz, we consider heating rates of $\dot{\bar{n}}_1 \approx 107$ and $\dot{\bar{n}}_2 \approx 22.5$ phonons per second for the center-of-mass and breathing modes, respectively. These heating rates are derived using data from Refs. [31,68] (for more details, check Appendix E). Using the aforementioned heating rates, starting from the ground state of motion, and with 64 pulses with $\Omega = (2\pi) \times 60$ kHz and $t_{\mathrm{FW}} = 7.72$ ms, the infidelity ($I = 1 - F$) increases from $I \approx 1.4 \times 10^{-4}$ to $I \approx 3 \times 10^{-4}$ to approximately equal to 3×10^{-4} when including heating in the model. This suggests that for Fig. 2(d) the heating of the motional modes may limit the infidelities to go below $I \approx 1.5 \times 10^{-4}$.

IV. PHASE-ADAPTIVE PULSE SEQUENCES

In this section, we show that an appropriate application of the global phase Φ on each DD block leads to enhanced robustness of the quantum gates that can be engineered in trapped-ion systems presenting longitudinal coupling. This is the main result of our work. In particular, we implement two approaches for selecting the phase of each DD block. These are, firstly, a scenario where the phase Φ is randomly chosen in each block [52] while, secondly, we consider a situation where the phases of successive DD blocks are correlated in different manners [53]. In our numerical simulations we incorporate the corrected final time, t_{FW}, that appears as a consequence of using realistic finite-width pulses (notice we introduce t_{FW} in the previous section). We anticipate that using the phase-adaptive method provides a significant enhancement in quantum-information-processing fidelities achieved by pulsed DD sequences, without adding a significant extra experimental complexity. Then our method is ready to be exploited in quantum platforms presenting longitudinal coupling, such as trapped ions and superconducting circuits.

Now, we present the basic mechanism leading to error cancelation by using the Φ phases. A single qubit under the effect of an imperfect MW field may be described by the following Hamiltonian:

$$H^I = \frac{\epsilon}{2}\sigma^z + \frac{\Omega + \delta\Omega}{2}(\sigma^+ e^{i\phi} + \sigma^- e^{-i\phi}), \tag{16}$$

where $\delta\Omega$ is constant shift in the Rabi frequency and ϵ accounts for a qubit frequency shift that may be produced by, for example, the variation of the intensity of the magnetic field B_0 or the effective coupling to other spins mediated by the collective motional modes. Like in the previous sections, in Eq. (16) the bosonic degrees of freedom are omitted as $\eta_{jm} \ll 1$.

The application of an imperfect π pulse is then characterized by the following matrix (see Appendix E for the

derivation):

$$U_\pi(\phi) = \begin{bmatrix} \sin\gamma & ie^{i(\phi-\beta)}\cos\gamma \\ ie^{-i(\phi-\beta)}\cos\gamma & \sin\gamma \end{bmatrix}. \quad (17)$$

Here we select $\Phi = 0$, while ϕ is the phase that determines the rotation axis—e.g., $\phi = 0\,(\pi/2)$ means a π pulse along the $X\,(Y)$ axis—and β and γ are real numbers related with ϵ and $\delta\Omega$. When the deviations are zero, Eq. (17) corresponds to a perfect π pulse.

A general DD pulse block (with an even number of pulses) results in

$$U_{\rm DD} = \begin{bmatrix} 1 & iC\gamma \\ iC^*\gamma & 1 \end{bmatrix} + O(\gamma^2). \quad (18)$$

Here, C is a complex number that depends on the structure of the employed DD block, see Ref. [52] for a detailed calculation. Repeating M times this DD block leads to

$$U = \begin{bmatrix} 1 & iMC\gamma \\ iMC^*\gamma & 1 \end{bmatrix} + O(\gamma^2). \quad (19)$$

Changing the global phase of all pulses in the DD block as $\Phi \to \Phi + \xi$ would change C in Eq. (18) to $Ce^{-i\xi}$. Then, if one choses different values for the phase Φ on each block (in the following we use Φ_s to denote the phase of the sth block) the matrix corresponding to an M-block sequence reads

$$U = \begin{bmatrix} 1 & iZ_M MC\gamma \\ iZ_M^* MC^*\gamma & 1 \end{bmatrix} + O(\gamma^2), \quad (20)$$

where $Z_M = 1/M \sum_{s=1}^{M} \exp(-i\Phi_s)$. The off-diagonal elements in Eqs. (19) and (20) are related with the robustness of the sequence in front of control errors. Essentially, if an even number of ideal π pulses is applied (this is, π pulses in the absence of errors) the off-diagonal elements must be zero. In Ref. [52] the randomization of the set of phases $\{\Phi_s\}$ was introduced to improve the performance of DD sequences for quantum sensing with N-V centers. More specifically, selecting random values for $\{\Phi_s\}$, induces a two-dimensional (2D) random walk in Z_M with a statistical variance $\langle |Z_M|^2 \rangle = 1/M < 1$. A further improvement for NMR detection purposes was introduced in Ref. [53]. Here, the phases $\{\Phi_s\}$ are chosen such that $\sum_{s=1}^{M} \exp(-i\Phi_s) = 0$ (this is, the phases are correlated). In this case $\langle |Z_M|^2 \rangle = 0$, thus the first-order dependence on the error parameter γ gets removed.

Now, we show that these techniques (originally conceived for quantum detection of nuclear spins) are useful in the context of quantum-information processing with trapped ions. For that, we concatenate ten XY8 blocks and evaluate the robustness of a Bell-state preparation protocol using different values for the phases Φ_s. We use Hamiltonian (10) as a starting point of our numerical simulations without doing any further approximation, while each bosonic mode starts at a thermal state with $\bar{n}_m = 1$. More specifically, we study the robustness of the Bell-state fidelity against errors in the energy of the qubits (or detuning errors) represented by ϵ, and deviations $\delta\Omega$ in the delivered Rabi frequencies.

The results are shown in Fig. 3. Note that we do not show the regions with negative ϵ as we find they are equivalent to those with positive ϵ. In particular, in Fig. 3(a), we sketch the evolution of the quantity Z_M in the complex plane, when all phases Φ_s take the same value. In Fig. 3(f), the Bell-state infidelity is shown as a function of

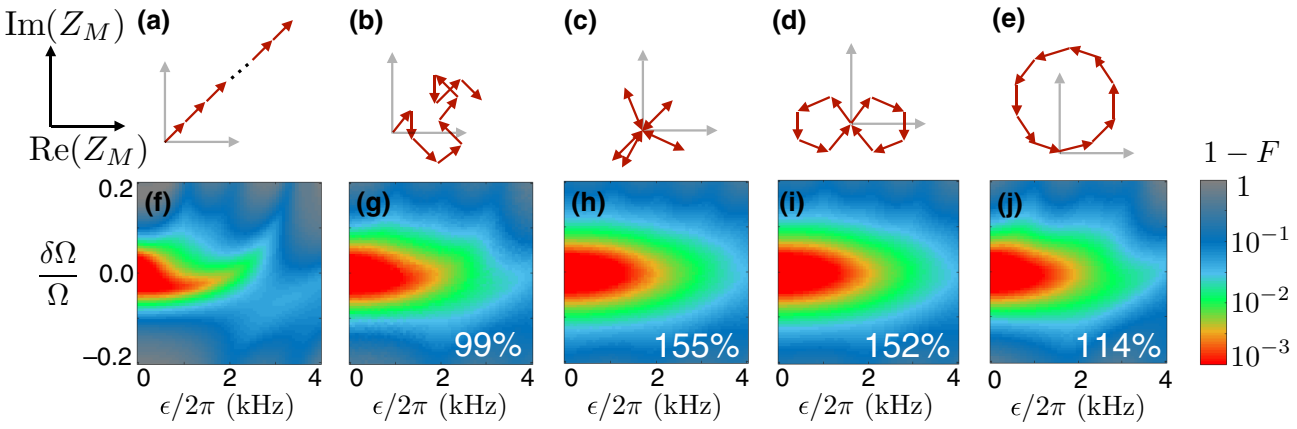

FIG. 3. XY8 pulse sequence with 80 pulses (i.e., ten XY8 blocks) and different choices for the value of the phases Φ_s. (a) Standard choice with $\Phi_s \equiv \Phi$. For each experimental run, Φ_s is chosen to be the same. (b) Full random phases. (c),(d),(e) Correlated phases where $\sum_{s=1}^{S} \exp(-i\Phi_s) = 0$ with $S = 2, 5$ and 10, respectively. In all cases, the first global phase Φ_1 is chosen randomly for each experimental run. (f)–(j) Results of the described pulse sequences in terms of the Bell-state infidelity for different values of the static control error $\delta\Omega$ and qubit frequency shift ϵ. The numbers in white represent how many more points with values above 99.9% fidelity are with respect to (f). For example, 100% would mean there are twice as many points that fulfil this condition compared with (f).

ϵ and $\delta\Omega$. The red region represents the highest Bell-state fidelities that can reach values above 99.9% for the following common experimental parameters: $\eta = 0.0113$, $\nu = (2\pi) \times 200$ kHz and $\Omega = (2\pi) \times 40$ kHz. In Fig. 3(b), a possible behavior is shown for Z_M when randomly selected phases Φ_s are employed. In this case, the robustness against control errors gets enhanced, as seen in Fig. 3(g). In particular, in Fig. 3(g) a larger region can be observed that presents fidelities on Bell-state preparation above 99.9%. More specifically, this region is 99% larger than that in Fig. 3(f). The latter corresponds to the application of the standard procedure where all phases Φ_s are equal. At this point we want to clarify that each point in Figs. 3(g)–3(j) corresponds to the average 20 different realizations, where in each realization a different set of phases Φ_s, random or correlated, is employed.

In Figs. 3(c)–3(e), we show Z_M for the cases where Φ_s are correlated such that $\sum_{s=1}^{S} \exp(-i\Phi_s) = 0$ with $S = 2, 5$ and 10, respectively. The performance of these sequences are shown in Figs. 3(h)–3(j). We find the largest fidelity enhancement with $S = 2$. Comparing this case with the standard procedure where all phases Φ_s are equal, our phase-adaptive method presents an improvement of 155%.

Phase-adaptive DD sequences can be directly applied to other schemes that make use of pulsed DD in trapped ions, for example, the one introduced in Ref. [51]. The DD sequence considered in Ref. [51] is the AXY-4 sequence, composed by four composite (each one formed by five π pulses) pulses. As, in this case, each experimental run makes use of a single DD block, phase randomization could be applied to all the different experimental runs. Then, by directly adding appropriate control on the phase on each DD block one can get significant improvements on quantum-information-processing fidelities.

V. CONCLUSIONS

We introduce phase-adaptive pulsed DD methods in the context of trapped ions with longitudinal coupling. We show that an optimal choice of the phases on each DD block leads to a significant enhancement in the robustness of entangling operations. This result has direct applications in quantum computing and simulation. Moreover, the enhancement achieved by our phase-adaptive method does not entail significant extra experimental cost, thus it can be easily incorporated to any pulsed DD method that aims to achieve robust quantum-information processing with trapped ions or with other systems presenting longitudinal coupling such as superconducting circuits.

ACKNOWLEDGMENTS

We acknowledge financial support from NSFC (Grant No. 12075145), SMSTC (Grants No. 2019SHZDZX01-ZX04, No. 18010500400, and No. 18ZR1415500), the Program for Eastern Scholar, Spanish Government via Grant No. PGC2018-095113-B-I00 (MCIU/AEI/FEDER, UE), Basque Government via IT986-16, as well as from QMiCS (Grant No. 820505) and (Grant No. 820363) of the EU Flagship on Quantum Technologies, and the EU FET Open Grant Quromorphic (Grant No. 828826). I.A. acknowledges the UPV/EHU Grant EHUrOPE. X.C. acknowledges the Ramón y Cajal program (RYC2017-22482) as well. This work is supported by Huawei HiQ funding for developing QAOA&STA (Grant No. YBN2019115204). J.C. acknowledges the Ramón y Cajal program (RYC2018-025197-I) and the EUR2020-112117 project of the Spanish MICINN, as well as support from the UPV/EHU through the Grant EHUrOPE.

APPENDIX A: INFIDELITY DUE TO RESIDUAL SPIN-BOSON COUPLING

In the following, we consider how ignoring Eq. (3) affects the generation of a Bell state. The fidelity between two states ρ_1 and ρ_2 is given by

$$F = \frac{|\mathrm{Tr}(\rho_1 \rho_2^\dagger)|}{\sqrt{\mathrm{Tr}(\rho_1 \rho_1^\dagger)\mathrm{Tr}(\rho_2 \rho_2^\dagger)}}. \tag{A1}$$

Thus, after a time $t = \pi/4J$, the Bell-state fidelity is

$$F = \frac{\left|\mathrm{Tr}\Big(\rho |B\rangle\langle B|\Big)\right|}{\sqrt{\mathrm{Tr}(\rho\rho^\dagger)}}, \tag{A2}$$

where $|B\rangle = \frac{1}{\sqrt{2}}(|++\rangle + i|--\rangle)$ with $|\pm\rangle_j = \frac{1}{\sqrt{2}}(|e\rangle_j \pm |g\rangle_j)$, and ρ is the final state. The latter is given by

$$\rho = \mathrm{Tr}_M\Big[U_F(t)(|B\rangle\langle B| \otimes \rho_T)U_F^\dagger(t)\Big], \tag{A3}$$

where ρ_T is the state of the motional modes, and Tr_M stands for a partial trace of all N motional subspaces. The matrix ρ can be rewritten as

$$\rho = \frac{1}{4}\begin{bmatrix} 1 & i\langle e^{g_2}\rangle & i\langle e^{g_1}\rangle & \langle e^{g_1+g_2}\rangle \\ -i\langle e^{-g_2}\rangle & 1 & \langle e^{g_1-g_2}\rangle & -i\langle e^{g_1}\rangle \\ -i\langle e^{-g_1}\rangle & \langle e^{-g_1+g_2}\rangle & 1 & -i\langle e^{g_2}\rangle \\ \langle e^{-g_1-g_2}\rangle & i\langle e^{-g_1}\rangle & i\langle e^{-g_2}\rangle & 1 \end{bmatrix}, \tag{A4}$$

up to a global phase, and where $g_j = 2\sum_m \alpha_{jm}(t)a_m^\dagger - \alpha_{jm}^*(t)a_m$, $g_j^\dagger = -g_j$, $[g_i, g_j] = 0$ and $\langle A\rangle = \mathrm{Tr}_M\Big(A\rho_T\Big)$.

Now, one can find that

$$\mathrm{Tr}\Big(\rho|B\rangle\langle B|\Big) = \frac{1}{4}\Big[1 + \langle\cosh(g_1)\rangle + \langle\cosh(g_2)\rangle + \langle\cosh(g_1)\cosh(g_2)\rangle\Big], \tag{A5}$$

and

$$\mathrm{Tr}\Big(\rho\rho^\dagger\Big) = \frac{1}{4}\Big(1 + \langle e^{g_1}\rangle\langle e^{-g_1}\rangle + \langle e^{g_2}\rangle\langle e^{-g_2}\rangle + \langle e^{g_1+g_2}\rangle\langle e^{-g_1-g_2}\rangle/2 + \langle e^{g_1-g_2}\rangle\langle e^{-g_1+g_2}\rangle/2\Big). \tag{A6}$$

If we assume that $|g_j| \ll 1$, one can expand the exponential and the hyperbolic cosine functions up to the fifth power of g_j. If ρ_T is a thermal state, the average value for odd powers of g_j will be zero. Using this, Eqs. (A5) and (A6) read

$$\mathrm{Tr}\Big(\rho|B\rangle\langle B|\Big) \approx 1 + x + y + O(g^6) \tag{A7}$$

and

$$\mathrm{Tr}\Big(\rho\rho^\dagger\Big) \approx 1 + 2x + z + O(g^6), \tag{A8}$$

where

$$\begin{aligned} x &= \frac{1}{4}(\langle g_i^2\rangle + \langle g_j^2\rangle), \\ y &= \frac{1}{3\times 2^4}(\langle g_i^4\rangle + \langle g_j^4\rangle) + \frac{1}{2^4}\langle g_i^2 g_j^2\rangle, \\ z &= \frac{1}{2^5}[2\langle g_i^2\rangle^2 + 2\langle g_j^2\rangle^2 + \langle(g_i+g_j)^2\rangle^2 + \langle(g_i-g_j)^2\rangle^2] \\ &\quad + \frac{1}{3\times 2^5}[2\langle g_i^4\rangle + 2\langle g_j^4\rangle + \langle(g_i+g_j)^4\rangle + \langle(g_i-g_j)^4\rangle]. \end{aligned} \tag{A9}$$

The fidelity can then be expanded as

$$F \approx (1 + x + y)(1 - x - z/2 + 3x^2/2), \tag{A10}$$

which gives

$$F \approx 1 - \frac{1}{2^5}(\langle g_i^2\rangle^2 + \langle g_j^2\rangle^2 + 4\langle g_i g_j\rangle^2). \tag{A11}$$

Using that $\langle g_j^2\rangle = -4\sum_m |\alpha_{jm}(t)|^2(2\bar{n}_m + 1)$ and $\langle g_i g_j\rangle = -4\sum_m \alpha_{im}(t)\alpha_{jm}^*(t)(2\bar{n}_m + 1)$, Eq. (A11) can be rewritten as

$$F \approx 1 - \frac{1}{2}\Big[\sum_{m,m'} \Theta_{mm'}(2\bar{n}_m + 1)(2\bar{n}_{m'} + 1)\Big], \tag{A12}$$

where

$$\Theta_{mm'} = |\alpha_{im}|^2|\alpha_{im'}|^2 + |\alpha_{jm}|^2|\alpha_{jm'}|^2 + 4\alpha_{im}\alpha_{jm}^*\alpha_{im'}\alpha_{jm'}^*. \tag{A13}$$

APPENDIX B: FIDELITY BOUND FOR A TWO-ION CRYSTAL

For $N = 2$, and assuming $\bar{n}_m = 1$, the fidelity formula in Eq. (7) becomes

$$F \approx 1 - \frac{9}{2}(\Theta_{11} + \Theta_{12} + \Theta_{21} + \Theta_{22}). \tag{B1}$$

If we assume that $\alpha_{jm}(t) = 2|\eta_{jm}|$, which maximizes the value of $\alpha_{jm}(t)$, we have that

$$F \lesssim 1 - 2^3 \times 9(\eta_{11}^4 + \eta_{21}^4 + 4\eta_{11}^2\eta_{21}^2 + 2\eta_{11}^2\eta_{12}^2 + 2\eta_{21}^2\eta_{22}^2 + 8\eta_{11}\eta_{12}\eta_{21}\eta_{22} + \eta_{12}^4 + \eta_{22}^4 + 4\eta_{12}^2\eta_{22}^2). \tag{B2}$$

As $\eta_{im} = b_{im}(\nu_m/\nu)^{-3/2} \times \eta$, then $\eta_{11} = \eta_{21} = 2^{-1/2}\eta$ and $\eta_{12} = -\eta_{22} = -2^{-1/2} \times 3^{-3/4}\eta$. Using these expressions, Eq. (B4) becomes

$$F \lesssim 1 - 2 \times 9(6 - 4 \times 3^{-3/2} + 6 \times 3^{-3})\eta^4, \tag{B3}$$

which can be approximately rewritten as

$$F \lesssim 1 - 98\eta^4. \tag{B4}$$

APPENDIX C: SPIN-SPIN COUPLING MATRIX

To characterize the ideal spin-spin Hamiltonian $H = \sum_{i,j} J_{ij}\sigma_i^z\sigma_j^z$ one has to calculate the spin-spin coupling matrix J_{ij}. This is given by $J_{ij} = \sum_m \nu_m\eta_{im}\eta_{jm}$, with $\eta_{im} = b_{im}(\nu_m/\nu)^{-3/2} \times \eta$. For $N = 2$, $\{\nu_1, \nu_2\} = \{1, \sqrt{3}\} \times \nu$, and

$$\begin{aligned} \vec{b}_1 &= \{0.7071, 0.7071\}, \\ \vec{b}_2 &= \{-0.7071, 0.7071\}, \end{aligned} \tag{C1}$$

where $\vec{b}_m \equiv \{b_{1m}, b_{2m}\}$. For $N = 6$, $\{\nu_1, \nu_2, \nu_3, \nu_4, \nu_5, \nu_6\} = \{1, \sqrt{3}, \sqrt{5.824}, \sqrt{9.352}, \sqrt{13.51}, \sqrt{18.27}\} \times \nu$, and

$$\begin{aligned}
\vec{b}_1 &= \{0.4082, 0.4082, 0.4082, 0.4082, 0.4082, 0.4082\},\\
\vec{b}_2 &= \{-0.6080, -0.3433, -0.1118, 0.1118, 0.3433, 0.6080\},\\
\vec{b}_3 &= \{-0.5531, 0.1332, 0.4199, 0.4199, 0.1332, -0.5531\},\\
\vec{b}_4 &= \{0.3577, -0.5431, -0.2778, 0.2778, 0.5431, -0.3577\},\\
\vec{b}_5 &= \{0.1655, -0.5618, 0.3963, 0.3963, -0.5618, 0.1655\},\\
\vec{b}_6 &= \{-0.0490, 0.2954, -0.6406, 0.6406, -0.2954, 0.0490\},
\end{aligned} \tag{C2}$$

with $\vec{b}_m \equiv \{b_{1m}, b_{2m}, b_{3m}, b_{4m}, b_{5m}, b_{6m}\}$ [57].

APPENDIX D: IMPROVED FIDELITY WITH A LARGER RABI FREQUENCY

Here, we use Hamiltonian (10) to demonstrate that improved fidelities are obtained when considering larger Rabi frequencies in the MW pulses. For that, we repeat the simulations done for Fig. 2(a) for the case $N = 6$, however, in this case we consider $\Omega = (2\pi) \times 160$ kHz. To avoid unwanted excitations of the motional modes, we increase the trapping frequency to $\nu = (2\pi) \times 440$ kHz, and lower the effective LD factor to $\eta = 0.008$. It can be observed that, unlike in Fig. 2(a), a fidelity close to 100% (above 99.99%) is reached in the limit $\epsilon \to 0$ (see Fig. 4).

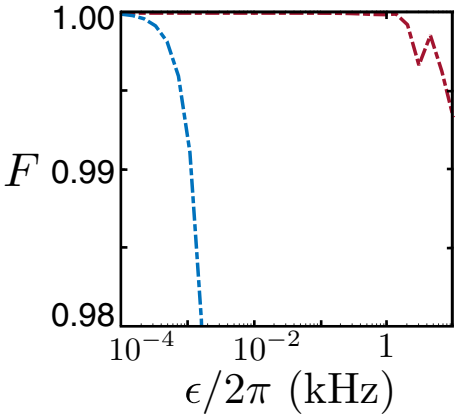

FIG. 4. Similar to Fig. 2(a), the fidelity with respect to the state generated by $H = \sum_{i,j} J_{ij}\sigma_i^z\sigma_j^z$ at $t_G = \pi/8 \max(|J_{ij}|)$ as a function of the strength of the unwanted shift ϵ and for $N = 6$ is shown. Here, for the pulsed case (dashed red) we consider a Rabi frequency of $\Omega = (2\pi) \times 160$ kHz, which results in a better fidelity than the case with $\Omega = (2\pi) \times 60$ kHz in Fig. 2(a) at the limit $\epsilon \to 0$.

APPENDIX E: DERIVATION OF THE HEATING RATES

Here we explain how the heating rates used in the main text are derived. As reference values, we use the $\dot{\bar{n}}_{1,\mathrm{ref}} \approx 41$ phonons/s reported for the center-of-mass mode with frequency $\nu_{1,\mathrm{ref}} = (2\pi) \times 426.7$ kHz [68], and the $\dot{\bar{n}}_{2,\mathrm{ref}} \approx 1.3$ phonons/s assumed in Ref. [31] for the breathing mode with frequency $\nu_{2,\mathrm{ref}} = (2\pi) \times \sqrt{3} \times 1.1$ MHz. In both cases, $g_B^{\mathrm{ref}} = 23.6$ T/m and the ion-electrode distance is $d_{\mathrm{ref}} = 310$ μm. To calculate the heating rates we use the following scaling relation [69]:

$$\dot{\bar{n}}_m \approx \dot{\bar{n}}_{m,\mathrm{ref}} \left(\frac{\nu_{m,\mathrm{ref}}}{\nu_m}\right)^2 \left(\frac{d_{\mathrm{ref}}}{d}\right)^4, \tag{E1}$$

and assume that $g_B \propto 1/d^2$.

APPENDIX F: IMPERFECT PULSE UNITARY

In an interaction picture with respect to $\Omega/2(\sigma^+ e^{i\phi} + \sigma^- e^{-i\phi})$, Hamiltonian (16) reads

$$H^{II}(t) = \frac{\epsilon}{2}\sigma^z e^{-i\Omega(t-t_0)\sigma^\phi} + \frac{\delta\Omega}{2}\sigma^\phi, \tag{F1}$$

where $\sigma^\phi = \sigma^+ e^{i\phi} + \sigma^- e^{-i\phi}$. If $t - t_0 = \pi/\Omega$, then the unitary evolution corresponding to Hamiltonian (16) is

$$U_\pi(\phi) = \exp(i\pi/2\sigma^\phi) \exp\left[-i\frac{\pi\Gamma}{2\Omega}\left(\frac{\epsilon}{\Gamma}\sigma^z + \frac{\delta\Omega}{\Gamma}\sigma^\phi\right)\right], \tag{F2}$$

where $\Gamma = \sqrt{\epsilon^2 + \delta\Omega^2}$. Using that, if $\hat{A}^2 = 1$, $e^{ia\hat{A}} = \cos(a) + i\sin(a)\hat{A}$, Eq. (F2) can be rewritten as

$$U_\pi(\phi) = i\sigma^\phi \begin{bmatrix} \cos\tilde{\Gamma} - i\frac{\epsilon}{\Gamma}\sin\tilde{\Gamma} & -i\frac{\delta\Omega}{\Gamma}\sin\tilde{\Gamma}e^{i\phi} \\ -i\frac{\delta\Omega}{\Gamma}\sin\tilde{\Gamma}e^{-i\phi} & \cos\tilde{\Gamma} + i\frac{\epsilon}{\Gamma}\sin\tilde{\Gamma} \end{bmatrix}, \tag{F3}$$

where $\tilde{\Gamma} = \pi\Gamma/2\Omega$. Equation (F3) can then be simplified to

$$U_\pi(\phi) = \begin{bmatrix} \sin\gamma & ie^{i(\phi-\beta)}\cos\gamma \\ ie^{-i(\phi-\beta)}\cos\gamma & \sin\gamma \end{bmatrix}, \tag{F4}$$

where $\sin\gamma = \delta\Omega/\Gamma \sin\tilde{\Gamma}$ and $\tan\beta = \epsilon/\Gamma \tan\tilde{\Gamma}$.

[1] M. A. Nielsen and I. L. Chuang, *Quantum Computation and Quantum Information* (Cambridge University Press, Cambridge, 2000).

[2] J. P. Dowling and G. J. Milburn, Quantum technology: The second quantum revolution, Philos. Trans. R. Soc. A **361**, 1655 (2003).

[3] A. Blais, A. L. Grimsmo, S. M. Girvin, and A. Wallraff, arXiv:2005.12667 [quant-ph].

[4] H. Häffner, C. F. Roos, and R. Blatt, Quantum computing with trapped ions, Phys. Rep. **469**, 155 (2008).

[5] D. Leibfried, R. Blatt, C. Monroe, and D. Wineland, Quantum dynamics of single trapped ions, Rev. Mod. Phys. **75**, 281 (2003).

[6] J. C. Bardin, D. H. Slichter, and D. J. Reilly, Microwaves in quantum computing, IEEE J. Microw. **1**, 403 (2021).

[7] C. J. Ballance, T. P. Harty, N. M. Linke, M. A. Sepiol, and D. M. Lucas, High-Fidelity Quantum Logic Gates Using Trapped-Ion Hyperfine Qubits, Phys. Rev. Lett. **117**, 060504 (2016).

[8] J. P. Gaebler, T. R. Tan, Y. Lin, Y. Wan, R. Bowler, A. C. Keith, S. Glancy, K. Coakley, E. Knill, D. Leibfried, and D. J. Wineland, High-Fidelity Universal Gate Set for $^{9}Be^{+}$ Ion Qubits, Phys. Rev. Lett. **117**, 060505 (2016).

[9] A. Friedenauer, H. Schmitz, J. T. Glueckert, D. Porras, and T. Schaetz, Simulating a quantum magnet with trapped ions, Nat. Phys. **4**, 757 (2008).

[10] K. Kim, M.-S. Chang, S. Korenblit, R. Islam, E. E. Edwards, J. K. Freericks, G.-D. Lin, L.-M. Duan, and C. Monroe, Quantum simulation of frustrated Ising spins with trapped ions, Nature **465**, 590 (2010).

[11] A. Bermudez, J. Almeida, F. Schmidt-Kaler, A. Retzker, and M. B. Plenio, Frustrated Quantum Spin Models with Cold Coulomb Crystals, Phys. Rev. Lett. **107**, 207209 (2011).

[12] J. W. Britton, B. C. Sawyer, A. C. Keith, C.-C. J. Wang, J. K. Freericks, H. Uys, M. J. Biercuk, and J. J. Bollinger, Engineered two-dimensional Ising interactions in a trapped-ion quantum simulator with hundreds of spins, Nature **484**, 489 (2012).

[13] R. Islam, C. Senko, W. C. Campbell, S. Korenblit, J. Smith, A. Lee, E. E. Edwards, C.-C. J. Wang, J. K. Freericks, and C. Monroe, Emergence and frustration of magnetism with variable-range interactions in a quantum simulator, Science **340**, 583 (2013).

[14] P. Jurcevic, B. P. Lanyon, P. Hauke, C. Hempel, P. Zoller, R. Blatt, and C. F. Roos, Quasiparticle engineering and entanglement propagation in a quantum many-body system, Nature **511**, 202 (2014).

[15] P. Richerme, Z.-X. Gong, A. Lee, C. Senko, J. Smith, M. Foss-Feig, S. Michalakis, A. V. Gorshkov, and C. Monroe, Non-local propagation of correlations in quantum systems with long-range interactions, Nature **511**, 198 (2014).

[16] R. Gerritsma, B. P. Lanyon, G. Kirchmair, F. Zähringer, C. Hempel, J. Casanova, J. J. García-Ripoll, E. Solano, R. Blatt, and C. F. Roos, Quantum Simulation of the Klein Paradox with Trapped Ions, Phys. Rev. Lett. **106**, 060503 (2011).

[17] M. Um, J. Zhang, D. Lv, Y. Lu, S. An, J.-N. Zhang, H. Nha, M. S. Kim, and K. Kim, Phonon arithmetic in a trapped ion system, Nat. Commun. **7**, 11410 (2016).

[18] Chr. Balzer, A. Braun, T. Hannemann, Chr. Paape, M. Ettler, W. Neuhauser, and Chr. Wunderlich, Electrodynamically trapped Yb^{+} ions for quantum information processing, Phys. Rev. A **73**, 041407(R) (2006).

[19] S. Olmschenk, K. C. Younge, D. L. Moehring, D. N. Matsukevich, P. Maunz, and C. Monroe, Manipulation and detection of a trapped Yb^{+} hyperfine qubit, Phys. Rev. A **76**, 052314 (2007).

[20] F. Mintert and C. Wunderlich, Ion-Trap Quantum Logic Using Long-Wavelength Radiation, Phys. Rev. Lett. **87**, 257904 (2001).

[21] J. Welzel, A. Bautista-Salvador, C. Abarbanel, V. Wineman-Fisher, C. Wunderlich, R. Folman, and F. Schmidt-Kaler, Designing spin-spin interactions with one and two dimensional ion crystals in planar micro traps, Eur. Phys. J. D **65**, 285 (2011).

[22] A. Khromova, Ch. Piltz, B. Scharfenberger, T. F. Gloger, M. Johanning, A. F. Varón, and Ch. Wunderlich, Designer Spin Pseudomolecule Implemented with Trapped Ions in a Magnetic Gradient, Phys. Rev. Lett. **108**, 220502 (2012).

[23] Ch. Piltz, T. Sriarunothai, S. S. Ivanov, S. Wölk, and C. Wunderlich, Versatile microwave-driven trapped ion spin system for quantum information processing, Sci. Adv. **2**, e1600093 (2016).

[24] S. Wölk and C. Wunderlich, Quantum dynamics of trapped ions in a dynamic field gradient using dressed states, New J. Phys. **19**, 083021 (2017).

[25] J. Welzel, F. Stopp, and F. Schmidt-Kaler, Spin and motion dynamics with zigzag ion crystals in transverse magnetic gradients, J. Phys. B: At., Mol. Opt. Phys. **52**, 025301 (2019).

[26] C. Ospelkaus, C. E. Langer, J. M. Amini, K. R. Brown, D. Leibfried, and D. J. Wineland, Trapped-Ion Quantum Logic Gates Based on Oscillating Magnetic Fields, Phys. Rev. Lett. **101**, 090502 (2008).

[27] C. Ospelkaus, U. Warring, Y. Colombe, K. R. Brown, J. M. Amini, D. Leibfried, and D. J. Wineland, Microwave quantum logic gates for trapped ions, Nature **476**, 181 (2011).

[28] H. Hahn, G. Zarantonello, M. Schulte, A. Bautista-Salvador, K. Hammerer, and C. Ospelkaus, Integrated $^{9}Be^{+}$ multi-qubit gate device for the ion-trap quantum computer, npj Quantum Inf. **5**, 70 (2019).

[29] G. Zarantonello, H. Hahn, J. Morgner, M. Schulte, A. Bautista-Salvador, R. F. Werner, K. Hammerer, and C. Ospelkaus, Robust and Resource-Efficient Microwave Near-Field Entangling $^{9}Be^{+}$ Gate, Phys. Rev. Lett. **123**, 260503 (2019).

[30] R. Srinivas, S. C. Burd, R. T. Sutherland, A. C. Wilson, D. J. Wineland, D. Leibfried, D. T. C. Allcock, and D. H. Slichter, Trapped-Ion Spin-Motion Coupling with Microwaves and a Near-Motional Oscillating Magnetic Field Gradient, Phys. Rev. Lett. **122**, 163201 (2019).

[31] S. Weidt, J. Randall, S. C. Webster, K. Lake, A. E. Webb, I. Cohen, T. Navickas, B. Lekitsch, A. Retzker, and W. K. Hensinger, Trapped-Ion Quantum Logic with Global Radiation Fields, Phys. Rev. Lett. **117**, 220501 (2016).

[32] B. Lekitsch, S. Weidt, A. G. Fowler, K. Mølmer, S. J. Devitt, C. Wunderlich, and W. K. Hensinger, Blueprint for a microwave trapped ion quantum computer, Sci. Adv. **3**, e1601540 (2017).

[33] C. F. Roos, Ion trap quantum gates with amplitude-modulated laser beams, New J. Phys. **10**, 013002 (2008).

[34] R. T. Sutherland, R. Srinivas, S. C. Burd, D. Leibfried, A. C. Wilson, D. J. Wineland, D. T. C. Allcock, D. H. Slichter,

and S. B. Libby, Versatile laser-free trapped-ion entangling gates, New J. Phys. **21**, 033033 (2019).
[35] N. Belmechri, L. Förster, W. Alt, A. Widera, D. Meschede, and A. Alberti, Microwave control of atomic motional states in a spin-dependent optical lattice, J. Phys. B: At., Mol. Phys. **46**, 104006 (2013).
[36] E. L. Hahn, Spin echoes, Phys. Rev. **80**, 580 (1950).
[37] H. Y. Carr and E. M. Purcell, Effects of diffusion on free precession in nuclear magnetic resonance experiments, Phys. Rev. **94**, 630 (1954).
[38] S. Meiboom and D. Gill, Modified spin-echo method for measuring nuclear relaxation times, Rev. Sci. Instrum. **29**, 688 (1958).
[39] A. Bermudez, P. O. Schmidt, M. B. Plenio, and A. Retzker, Robust trapped-ion quantum logic gates by continuous dynamical decoupling, Phys. Rev. A **85**, 040302(R) (2012).
[40] A. Lemmer, A. Bermudez, and M. B. Plenio, Driven geometric phase gates with trapped ions, New J. Phys. **15**, 083001 (2013).
[41] I. Cohen, S. Weidt, W. K. Hensinger, and A. Retzker, Multi-qubit gate with trapped ions for microwave and laser-based implementation, New J. Phys. **17**, 043008 (2015).
[42] R. Puebla, J. Casanova, and M. B Plenio, A robust scheme for the implementation of the quantum Rabi model in trapped ions, New J. Phys. **18**, 113039 (2016).
[43] I. Arrazola, M. B. Plenio, E. Solano, and J. Casanova, Hybrid Microwave-Radiation Patterns for High-Fidelity Quantum Gates with Trapped Ions, Phys. Rev. Appl. **13**, 024068 (2020).
[44] G. A. Álvarez and D. Suter, Measuring the Spectrum of Colored Noise by Dynamical Decoupling, Phys. Rev. Lett. **107**, 230501 (2011).
[45] N. Bar-Gill, L. M. Pham, C. Belthangady, D. Le Sage, P. Cappellaro, J. R. Maze, M. D. Lukin, A. Yacoby, and R. Walsworth, Suppression of spin-bath dynamics for improved coherence of multi-spin-qubit systems, Nat. Commun. **3**, 858 (2012).
[46] J. Casanova, Z.-Y. Wang, J. F. Haase, and M. B. Plenio, Robust dynamical decoupling sequences for individual-nuclear-spin addressing, Phys. Rev. A **92**, 042304 (2015).
[47] I. Baumgart, J.-M. Cai, A. Retzker, M. B. Plenio, and Ch. Wunderlich, Ultrasensitive Magnetometer Using a Single Atom, Phys. Rev. Lett. **116**, 240801 (2016).
[48] I. Arrazola, E. Solano, and J. Casanova, Selective hybrid spin interactions with low radiation power, Phys. Rev. B **99**, 245405 (2019).
[49] C. Munuera-Javaloy, I. Arrazola, E. Solano, and J. Casanova, Double quantum magnetometry at large static magnetic fields, Phys. Rev. B **101**, 104411 (2020).
[50] T. P. Harty, M. A. Sepiol, D. T. C. Allcock, C. J. Ballance, J. E. Tarlton, and D. M. Lucas, High-Fidelity Trapped-Ion Quantum Logic Using Near-Field Microwaves, Phys. Rev. Lett. **117**, 140501 (2016).
[51] I. Arrazola, J. Casanova, J. S. Pedernales, Z.-Y. Wang, E. Solano, and M. B. Plenio, Pulsed dynamical decoupling for fast and robust two-qubit gates on trapped ions, Phys. Rev. A **97**, 052312 (2018).
[52] Z.-Y. Wang, J. E. Lang, S. Schmitt, J. Lang, J. Casanova, L. McGuinness, T. S. Monteiro, F. Jelezko, and M. B. Plenio, Randomization of Pulse Phases for Unambiguous and Robust Quantum Sensing, Phys. Rev. Lett. **122**, 200403 (2019).
[53] Z.-Y. Wang, J. Casanova, and M. B. Plenio, Enhancing the robustness of dynamical decoupling sequences with correlated random phases, Symmetry **12**, 730 (2020).
[54] V. E. Manucharyan, J. Koch, L. I. Glazman, and M. H. Devoret, Fluxonium: Single Cooper-pair circuit free of charge offsets, Science **326**, 113 (2009).
[55] S. Richer and D. DiVincenzo, Circuit design implementing longitudinal coupling: A scalable scheme for superconducting qubits, Phys. Rev. B **93**, 134501 (2016).
[56] S. Jain, J. Alonso, M. Grau, and J. P. Home, Scalable Arrays of Micro-Penning Traps for Quantum Computing and Simulation, Phys. Rev. X **10**, 031027 (2020).
[57] D. F. V. James, Quantum dynamics of cold trapped ions with application to quantum computation, Appl. Phys. B **66**, 181 (1998).
[58] C. Wunderlich, Conditional spin resonance with trapped ions, *Laser Physics at the Limit* (Springer, Berlin, Heidelberg, 2002).
[59] D. Porras and J. I. Cirac, Effective Quantum Spin Systems with Trapped Ions, Phys. Rev. Lett. **92**, 207901 (2004).
[60] E. Ising, Beitrag zur theorie des ferromagnetismus, Z. Phys. **31**, 253 (1925).
[61] N. Hatano and M. Suzuki, *Quantum Annealing and Other Optimization Methods* (Springer, Berlin, 2005), p.37.
[62] S. Zippilli, M. Johanning, S. M. Giampaolo, Ch. Wunderlich, and F. Illuminati, Adiabatic quantum simulation with a segmented ion trap: Application to long-distance entanglement in quantum spin systems, Phys. Rev. A **89**, 042308 (2014).
[63] I. Arrazola, J. S. Pedernales, L. Lamata, and E. Solano, Digital-analog quantum simulation of spin models in trapped ions, Sci. Rep. **6**, 30534 (2016).
[64] Ch. Piltz, B. Scharfenberger, A. Khromova, A. F. Varón, and Ch. Wunderlich, Protecting Conditional Quantum Gates by Robust Dynamical Decoupling, Phys. Rev. Lett. **110**, 200501 (2013).
[65] F. Haddadfarshi and F. Mintert, High fidelity quantum gates of trapped ions in the presence of motional heating, New J. Phys. **18**, 123007 (2016).
[66] A. E. Webb, S. C. Webster, S. Collingbourne, D. Bretaud, A. M. Lawrence, S. Weidt, F. Mintert, and W. K. Hensinger, Resilient Entangling Gates for Trapped Ions, Phys. Rev. Lett. **121**, 180501 (2018).
[67] Y. Shapira, R. Shaniv, T. Manovitz, N. Akerman, and R. Ozeri, Robust Entanglement Gates for Trapped-Ion Qubits, Phys. Rev. Lett. **121**, 180502 (2018).
[68] S. Weidt, J. Randall, S. C. Webster, E. D. Standing, A. Rodriguez, A. E. Webb, B. Lekitsch, and W. K. Hensinger, Ground-State Cooling of a Trapped Ion Using Long-Wavelength Radiation, Phys. Rev. Lett. **115**, 013002 (2015).
[69] M. Brownnutt, M. Kumph, P. Rabl, and R. Blatt, Ion-trap measurements of electric-field noise near surfaces, Rev. Mod. Phys. **87**, 1419 (2015).